Variable Angle-of-Attack Profile Entry Guidance for a Crewed Lifting Body

Zachary R. Putnam*, Michael J. Grant†, Jenny R. Kelly‡, and Robert D. Braun§
Georgia Institute of Technology, Atlanta, Georgia, 30332

Zachary C. Krevor¶
Sierra Nevada Corporation, Louisville, Colorado, 80027

The feasibility of flying a crewed lifting body, such as the HL-20, during entry from low-Earth orbit without steady-state body flap deflections was evaluated. This entry strategy mitigates the severity of the aerothermal environment on the vehicle's body flaps and reserves control power for transient maneuvers. A numeric predictor-corrector entry guidance algorithm was developed to accommodate the range of vehicle trim angle-of-attack profiles possible when steady-state body flap deflections are prohibited. Results show that the guidance algorithm is capable of steering the vehicle to a desired target from low-Earth orbit while satisfying a reasonable suite of trajectory constraints, including limits on peak heat rate, peak sensed deceleration, and integrated heat load. Uncertainty analyses confirm this result and show that the vehicle maintains significant performance robustness to expected day-of-flight uncertainties. Additionally, parametric scans over mission design parameters of interest indicate a high level of flexibility is available for the low-Earth orbit return mission. Together, these results indicated that the proposed entry strategy is feasible: crewed lifting bodies may be effectively flown without steady-state body flap deflections.

Nomenclature

$\mathbf{a}$	Sensed acceleration vector, ft/s^2	r	Position vector magnitude, ft
a	Sensed acceleration vector magnitude, ft/s^2	S_{ref}	Aerodynamic reference area, ft^2
C_D	Drag coefficient	t	Time, s
C_L	Lift coefficient	$\mathbf{v}$	Velocity vector, ft/s
C_M	Pitch moment coefficient	v	Velocity vector magnitude, ft/s
D	Drag force magnitude, lb	α	Angle of attack, rad
F	Correction factor	Δ	Change in parameter
K	Filter gain	γ	Geodetic flight-path angle, rad
L	Lift force magnitude, lb	ϕ	Bank angle, rad
L/D	Lift-to-drag ratio	μ	Gravitational parameter, ft^3/s^s
m	Mass, slug	ω	Earth rotation rate, rad/s
M	Mach number	ρ	Atmospheric density, slug/ft^3
$\mathbf{r}$	Position vector, ft	θ	Downrange subtended angle, rad

*Graduate Research Assistant, School of Aerospace Engineering, 270 Ferst Drive, Senior Member AIAA.
†Graduate Research Assistant, School of Aerospace Engineering, 270 Ferst Drive, Member AIAA.
‡Research Engineer, School of Aerospace Engineering, 270 Ferst Drive, Member AIAA.
§Professor, School of Aerospace Engineering, 270 Ferst Drive, AIAA Fellow.
¶Principal Systems Engineer, 1722 Boxelder Street, Suite 102, Senior Member AIAA.

Subscript

cmd	Command	*nom*	Nominal
est	Estimate	*rel*	Earth-relative frame
i	Index	*w*	Wind-relative frame

I. Introduction

LIFTING body entry vehicles provide several advantages over blunt body capsules for human return from low-Earth orbit (LEO), where mission design flexibility and minimizing crew recovery time are important operational goals. Relative to capsules, lifting bodies possess high hypersonic lift-to-drag ratios which enable low peak deceleration entries and provide significant crossrange capability. This crossrange capability directly improves landing opportunity frequency from LEO. Lifting bodies may also perform runway landings, simplifying recovery and eliminating the need for parachutes or terminal deceleration systems.

The HL-20 lifting body was developed for the Personnel Launch System by the NASA Langley Research Center in the early 1990s and was intended to provide a round-trip crew transport capability to LEO, including what is now the International Space Station (ISS) (see Fig. 1).[1] When returning crew from LEO, the HL-20 was to utilize reaction control system (RCS) jets and aerosurfaces to perform a low-g entry followed by a runway landing. This approach allowed immediate access to crew and cargo after landing. An insulating thermal protection system (TPS) was baselined to maximize vehicle reusability.

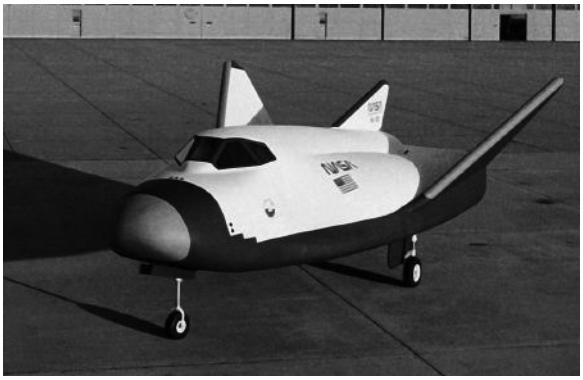

Figure 1. NASA HL-20 Personnel Launch System lifting body.[1]

The HL-20's two lower body flaps (LBFs) are the primary aerosurfaces used for α control (through steady-state deflections) and bank angle control (through differential deflections). Large steady-state LBF deflections near peak heating during entry may increase the severity of the local aerothermal environment on the LBFs. This is of particular concern for insulating TPS, which typically require heat rate and surface temperature to be limited during entry. Two possible strategies could be pursued to mitigate these aerothermal concerns: design the LBF TPS such that the predicted surface temperatures are accommodated or design the entry flight profile such that large LBF deflections are not required. Accommodating the predicted surface temperatures associated with large LBF deflections implies either utilizing a high-temperature LBF TPS or increasing LBF size to achieve the same control power at lesser deflections; both of these hardware solutions add cost and mass to the vehicle. Adopting a flight profile with minimal LBF deflections has the potential to reduce the severity of the aerothermal environment, while precluding hardware accommodations or minimizing their magnitude, as well as the associated vehicle costs and mass impacts.

The entry flight profile is determined by the onboard guidance algorithm. Heritage lifting body entry guidance algorithms, such as the Space Transportation System (STS) orbiter entry guidance algorithm, use pre-computed drag profiles based on a specified α profile to steer towards a target while keeping the vehicle within a prescribed entry corridor.[2] The entry corridor is defined by relevant trajectory constraints, including limits on deceleration, heat rate, and integrated heat load. This type of algorithm was well suited to the STS: the orbiter's large body flap was used to maintain the required α profile. However, the requirement to follow a specific α profile in all scenarios may require large steady-state LBF deflections for a HL-20 type lifting body. This is caused by the difference between the required and undeflected α profiles, as well as predicted uncertainties in the vehicle center of gravity (c.g.) position and C_M. Figure 2(a) shows the STS guidance algorithm α profile[2] and three undeflected trim α profiles for an HL-20-like lifting body with a nominal trim L/D near 1: nominal, minimum-L/D stress case, and maximum-L/D stress case. The stress cases are described in more detail in Section IV.A. The differences in these α profiles indicate that body flaps must be used if a single α profile is to be used. Figure 2(b) shows the LBF deflections required to achieve a single trim-α profile. This trim-α profile corresponds to the maximum-L/D case because the LBFs

can only deflect downward and so are only capable of decreasing trim α. These results show that a range of trim-α profiles must be accommodated to reduce LBF deflection during entry.

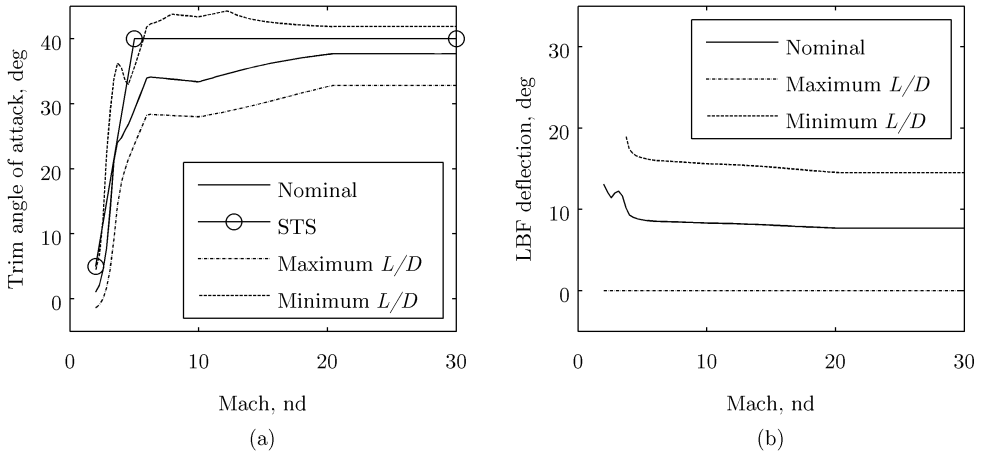

Figure 2. HL-20-like lifting body (a) trim-α profiles and (b) associated LBF-deflection profiles.

This study assesses the feasibility of a new entry strategy in which a lifting body based on the HL-20 is flown at undeflected-LBF trim attitudes. A numeric predictor-corrector (NPC) architecture was selected for the guidance algorithm used in this feasibility assessment. NPC-based algorithms offer several advantages over STS-like reference following algorithms. NPC-based algorithms are conceptually simple: the predictor-corrector loop typically solves a root finding problem and can easily accommodate nonlinear functions. NPC-based algorithms also provide a flexible, model-based guidance framework in which new constraints or trajectory shaping goals may be added without extensive modification to the core algorithm and the physical models of the environment and vehicle. Finally, NPC algorithms may be easily tailored to provide the required balance between accuracy and onboard computational resource requirements.

The primary costs associated with using a NPC-based algorithm are onboard computational resource requirements and software complexity. However, modern flight computers provide more than enough computational throughput for NPCs, provided algorithm performance is well defined and appropriate guidance rates are used. NPC software complexity also does not typically exceed that of other onboard mission critical software. The feasibility of flying such an algorithm is supported by past concepts and current programs: a NPC algorithm was considered for the Aeroassist Flight Experiment in the 1980s using a then-current flight computer,[3] the PredGuid NPC was selected for use on the Orion Crew Exploration Vehicle for skip entry lunar return,[4] and a modified version of PredGuid will be used for the upcoming Orion Multipurpose Crew Vehicle Entry Flight Test in 2014.[5]

II. Methodology

A. Numeric Simulation

Vehicle performance was determined using a three-degree-of-freedom numeric simulation. Vehicle attitude was modeled with a static trim calculation about the pitch axis; vehicle dynamics about the roll and yaw axes were not modeled. This strategy removed the need to develop a flight control system and enabled a rapid assessment of the primary question of interest: the feasibility of flying the assumed lifting body at undeflected trim-α profiles to reduce LBF deflections.

The trajectory simulation used to conduct the analyses for this feasibility study is written in Matlab, autocoded to C, and compiled to improve execution speed. The equations of motion are integrated using a 4th-order Runge-Kutta integration scheme with a constant time step of 0.05 s. The Earth is modeled as a rotating oblate spheroid. Range over the Earth's surface is computed using Vincenty's method.[6] Gravity is modeled using an inverse square law with J2 perturbations. The atmosphere is modeled using a table lookup, where atmospheric properties are stored as a function of altitude. The atmosphere table data were generated using the Global Reference Atmosphere Model (GRAM) 2007 version 1.4 with default settings.[7]

Convective heating is computed for a 1 ft reference sphere using Chapman's equation.[8] Radiative heating is assumed to be negligible for the entry velocities and energies associated with return from LEO.[9] Specific environment model parameters used in the simulation are given in Table 1.

B. Vehicle Model

The entry vehicle used in this study is based on NASA's HL-20 lifting body but also incorporates modern technology upgrades. The entry vehicle was modeled as a constant mass body with Mach- and α-dependent aerodynamics. A static trim calculation was used at each simulation major time step to determine the current α and corresponding aerodynamic properties using aerodynamics data from the HL-20.[10] Changes in aerodynamic properties due to aerosurface deflections were not considered in this study—it was assumed that transient effects from bank maneuvers and other disturbances can be damped quickly by the flight control system and that such transients have a negligible effect on overall vehicle performance. Changes in α computed by the static trim calculation were assumed to be instantaneous; non-zero sideslip angles and asymmetric flight conditions were not considered.

Table 1. Simulation Model Parameters

Parameter	Value
Equatorial radius, ft	2.0926×10^7
Polar radius, ft	2.0856×10^7
Rotation rate, rad/s	7.2921×10^{-5}
Grav. param., ft^3/s^2	1.4076×10^{16}
J2 perturbation	1.0826×10^{-3}
Atmosphere	GRAM 2007 v1.4
Chapman coeff., $slug^{\frac{1}{2}}/ft$	1.46×10^{-5}

Vehicle mass was assumed to be 534.28 slug, 10% less than that of the HL-20 Personnel Launch System mass.[11] This reduction reflects the mass saving technologies incorporated into a modern version of the HL-20 discussed in Ref. 12. The lifting body was assumed to be 31 ft long with a wingspan of 23.5 ft.[13] S_{ref} was assumed to be 323.27 ft^2 and is based on the planform area of the vehicle excluding the tip fins.[10] The nominal c.g. location was chosen such that the undeflected nominal hypersonic trim L/D was near 1 at Mach 25. The flight control system and effectors were approximated with bank angle rate and acceleration limits. Bank angle rates were limited to 20 deg/s. The RCS bank acceleration was limited to 1.5 deg/s^2. The aerosurface bank acceleration was limited to 2.5 deg/s^2, which corresponds to approximately 10 deg deflection limits for the LBFs. This is the maximum deflection for which acceptable LBF temperatures are not exceeded during entry. A linear bridging function was used to model the RCS-to-aerosurface effector transition between dynamic pressures of 2 and 60 lb/ft^2. The flight computer was modeled with a low rate group for guidance, running at 0.5 Hz, and a medium rate group for flight control, running at 10 Hz. Onboard navigation knowledge was assumed to be perfect.

C. Mission Design

The primary mission considered for this study was returning crew from the ISS to the Shuttle Landing Facility at Kennedy Space Center (KSC), located at (28.60 deg N, 279.32 deg E). The nominal entry interface (EI) states are given in Table 2 for both ascending and descending approaches to KSC. These EI states represent potential deorbit targets from the nominal ISS orbit (circular, inclination of 51.6 deg, mean altitude of 200 nmi) when a single impulsive deorbit burn of 328 ft/s is used. Simulations started at EI, defined to be at 400,000 ft altitude, and were terminated at a terminal area energy management (TAEM) initiation velocity of2,500 ft/s, the same velocity used by the STS algorithm.[2] The nominal ascending and descending approach trajectories have entry ranges of approximately 4,830 and 4,920 nmi, respectively. These entry ranges were selected to position the target landing site near the center of the vehicle's downrange capability for each EI state.

Several constraints influenced the selection of these EI states. Operational trajectory constraints included a peak heat rate limit of 80 $BTU/s/ft^2$ and an integrated heat load limit of 100,000 BTU/ft^2. These numbers are consistent with the aerodynamic heating environment identified for the HL-20 in Ref. 14. A peak deceleration limit of 4 g was used. This value is consistent with the launch deceleration limit in Ref. 12 and ensures compliance with NASA's duration-based acceleration limits for ill or deconditioned crew specified in the Human-System Integration Requirements.[15] Lastly, the STS accuracy requirement at TAEM initiation was imposed: trajectories reaching the TAEM transition velocity within 5 nmi of the target location were considered acceptable.[2]

Table 2. Nominal Entry Interface States

Parameter	Ascending approach	Descending approach
Geodetic altitude, ft	400,000	400,000
Geodetic latitude, deg N	-35.81	40.07
Longitude, deg E	226.25	173.35
Earth-relative velocity magnitude, ft/s	24,899.0	24,895.7
Earth-relative geodetic flight-path angle, deg (positive above local horizontal)	-1.36	-1.36
Earth-relative geodetic azimuth angle, deg	47.96	52.43

D. Monte Carlo Simulation

Monte Carlo simulations were conducted to evaluate vehicle performance in the presence of day-of-flight uncertainties. Monte Carlo simulations in this study used 1,000 samples. The input uncertainty distributions are given in Table 3. Uniform distributions were used to provide additional conservatism in the analyses when distributions were not available in the literature. Dispersed atmosphere tables were generated using the GRAM 2007 version 1.4 correlated uncertainty models. Symmetric aerodynamic dispersions were stored as a function of Mach number and applied using dispersed scalar multipliers between -1 and 1. EI state dispersions were taken from Project Orion.[4] These estimates are likely conservative, as they are based on a final trajectory correction maneuver performed five hours prior to EI,[16] a much longer time for error growth than will occur for a lifting body after a deorbit burn. EI state uncertainties were assumed to be uncorrelated, providing additional conservatism. Only delivery errors were modeled—the navigation system was assumed to have perfect knowledge of vehicle dynamics. Center-of-gravity dispersions are conservative estimates derived from scaling STS c.g. uncertainties.[17]

Table 3. Monte Carlo Simulation Inputs

Parameter	Distribution
Atmosphere	GRAM 2007 v1.4 dispersions
EI latitude	Uniform, ±0.2 deg, Ref. 4
EI longitude	Uniform, ±0.2 deg, Ref. 4
EI altitude	Uniform, ±500 ft, Ref. 4
EI velocity mag.	Gaussian, std. dev. of 30 ft/s, Ref. 4
EI flight-path	Gaussian, std. dev. of 0.033 deg, Ref. 4
EI azimuth	Uniform, ±0.025 deg, Ref. 4
Vehicle mass	Uniform, ±3%, Ref. 4
X c.g. position	Uniform, ±1.5 in, estimate based on Ref. 17
Z c.g. position	Uniform, ±1.0 in
Y c.g. position	None (lateral dynamics not modeled)
Bank acceleration	RCS: uniform, ±0.5 deg/s^2 Aerosurfaces: uniform, ±1 deg/s^2
ΔC_L multiplier	Uniform, ±1
ΔC_D multiplier	Uniform, ±1
ΔC_M multiplier	Uniform, ±1

III. Guidance Algorithm

Traditionally, entry guidance algorithms are designed to deliver a vehicle (e.g. Space Shuttle Orbiter, HL-20) from space to a target location on the Earth's surface using bank angle steering. In this approach, the drag experienced by the vehicle is controlled by the vertical component of lift such that the predicted flight range of the vehicle is consistent with the range to the target. During this targeting process, α is typically commanded to a pre-set, near-constant profile.[2,11] Following the α profile closely during entry limits the range of aerodynamic properties possible during flight, allowing the use of analytic guidance algorithms based on linearization of the equations of motion to perform targeting. As discussed in Section I, the large steady-state LBF deflections required for this type of guidance approach lead to increased heating on the LBFs. An NPC-based guidance algorithm was developed to accommodate entry flight with undeflected LBFs and the resultant range of trim-α profiles and their associated aerodynamic properties.

To limit the use of onboard computational resources, longitudinal (downrange) and lateral (crossrange) guidance commands are fully decoupled, allowing the use of planar equations of motion for numeric downrange prediction. The NPC provides the targeting capability for the longitudinal channel. Real-time estimation is used to improve the accuracy of the numeric predictions.

A. Numeric Predictor-Corrector

1. Predictor

A modified set of planar equations of motion given by Eq. (1) are propagated forward in time to predict downrange. Eq. (1c) includes an additional term, F_c, that corrects for the Coriolis effect. The guidance algorithm will under predict the downrange without this correction. This effect is not included in the planar equations of motion since it cannot be calculated from the planar states alone. However, the navigation system still provides a three-degree-of-freedom vehicle state estimate that can be used to approximate the component of the Coriolis effect within the plane of motion as shown in Eq. (2).

$$\frac{dr}{dt} = v\sin\gamma \tag{1a}$$

$$\frac{dv}{dt} = -\frac{D}{m} - \frac{\mu\sin\gamma}{r^2} \tag{1b}$$

$$\frac{d\gamma}{dt} = \frac{L\cos(\phi) + F_c}{mv} + \left(\frac{v}{r} - \frac{\mu}{vr^2}\right)\cos\gamma \tag{1c}$$

$$\frac{d\theta}{dt} = \frac{v\cos\gamma}{r} \tag{1d}$$

F_c is approximated by assuming that the Earth-relative velocity vector direction remains constant in the plane of motion during each guidance prediction. This assumption is reasonable during hypersonic flight where the changes in flight-path angle are small; it enables a computationally efficient and effective approximation of the Coriolis effect. The negative sign results from the treatment of the Coriolis effect as a force.

$$F_c = -\frac{2m}{\cos\gamma}\left(\omega \times \frac{\mathbf{v}_{rel}}{\|\mathbf{v}_{rel}\|} v_{planar}\right) \cdot \frac{\mathbf{r}_{rel}}{\|\mathbf{r}_{rel}\|} \tag{2}$$

Eq. (1) are propagated using a 4th-order Runge-Kutta integration scheme with a constant time step of 2 s using a constant bank angle command. Propagations at terminated at 2,500 ft/s relative velocity (TAEM initiation). A spherical Earth is assumed with a nominal atmosphere profile. Vehicle aerodynamic properties are estimated for each prediction as described in Section D. Range is calculated relative to the great circle that connects the target location to the vehicle location at targeting initiation.

2. Corrector

Using a constant bank command reduces the downrange targeting problem to a one-dimensional search: finding the constant bank angle that results in a trajectory that nulls the range error at TAEM initiation. The corrector performs this one-dimensional search while attempting to satisfy all entry trajectory constraints.

Corrector algorithms often trade computational predicability (e.g., using zero-order methods such as bisection) with convergence rate (e.g., using first-order methods such as secant).[4,18] For well-conditioned targeting problems that frequently occur late in entry, first-order methods rapidly converge. However, sensitive targeting problems that frequently occur early in entry, when the vehicle has substantial downrange control authority, may require many iterations when first-order methods are used. These highly sensitive targeting problems can be solved in fewer iterations with zero-order methods. Therefore, the corrector nulls the range error using Brent's method, which combines both zero- and first-order methods through the use of the bisection method, secant method, and inverse quadratic interpolation.[19] This approach ensures that a solution is reliably identified within a set number of iterations while providing the possibility of faster convergence through the use of the secant method and inverse quadratic interpolation.

A correction tolerance of 0.1 deg in bank angle is used to terminate the NPC loop for the current guidance cycle. The resulting bank angle is passed through a first-order filter, shown in Eq. (3), where $\phi_{cmd,i}$ is the current commanded bank angle, $\phi_{cmd,i-1}$ is the prior commanded bank angle, ϕ_i is the bank angle obtained by the NPC, and K is the filter gain. A K value of 0.8 provides a balance between variability and responsiveness in the bank command.

$$\phi_{cmd,i} = (1 - K)\phi_{cmd,i-1} + K \cdot \phi_i \tag{3}$$

B. Longitudinal Guidance Phases

Longitudinal guidance is split into four consecutive, functional phases: pull-out, energy depletion, downrange targeting, and heading alignment.

1. Pull-Out Phase

During the first phase of entry, the pull-out phase commands full lift up to arrest the descent rate of the vehicle and prevent violations of the heat rate constraint as shown in Fig. 3(a).[20] The pull-out phase is terminated when the Earth-relative flight-path angle is greater than -0.3 deg, a sufficiently shallow angle to avoid heat rate constraint violations. This criterion provides a smooth transition to the energy depletion phase. The vehicle location at the transition to the energy depletion phase is recorded to construct a great circle used as a reference for downrange computations.

2. Energy Depletion Phase

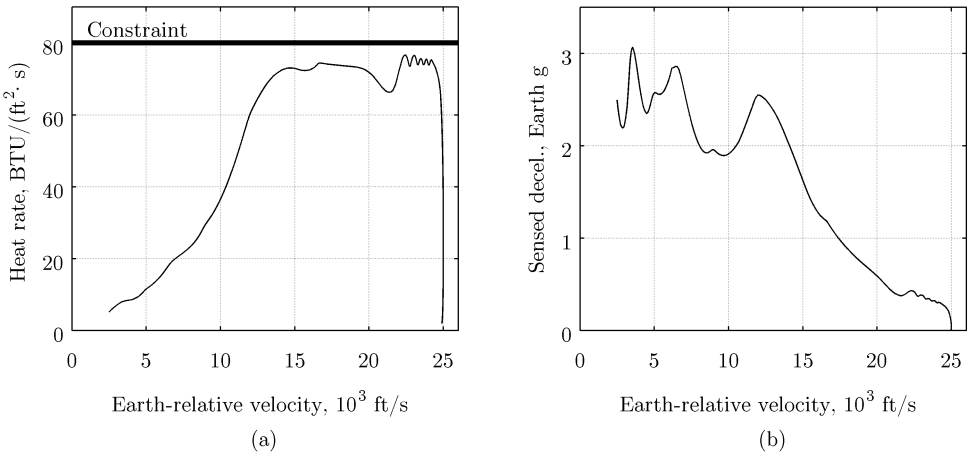

Figure 3. Example entry trajectories: (a) the pull-out and energy depletion phases limit the peak heat rate; (b) increased g-loading in latter portion of entry.

To prevent excessive g-loading near the end of the trajectory, as shown in the example in Fig. 3(b), the maximum possible amount energy is depleted early in entry. However, the depletion rate is limited by the heat rate constraint. Therefore, the guidance algorithm commands the vehicle to fly along the heat rate

constraint, using a stand-off distance of 5 BTU/(ft^2·s) to prevent violations of the heat rate constraint. This energy depletion phase is critical for α profiles that result in low-C_D and high-L/D values. Without sufficient deceleration early in the trajectory, these cases tend to overshoot the target or violate the deceleration constraint late in the trajectory.

During the energy depletion phase, the NPC is used to identify a constant bank angle command that keeps the vehicle near the heat rate constraint. Tracking of the heat rate constraint continues until the vehicle meets two criteria: a velocity gate that is a function of the estimated drag coefficient as given in Eq. (4) and a delay timer that is a function of the estimated L/D, given by Eq. (5). Together, the velocity gate and delay timer ensure that a sufficient amount of energy is depleted such that excessive g-loading near the end of the trajectory is avoided. The HL-20 was capable of implementing a linear feedback controller to follow the heat rate constraint by maintaining a near-constant α.[20] However, the absence of α control introduces nonlinearities into the dynamics, making that approach infeasible. After the vehicle passes through the velocity gate and satisfies the delay timer, the guidance algorithm transitions to the downrange targeting phase.

$$v_{gate} = \begin{cases} 24,000 \text{ ft/s} & : C_D > 0.5 \\ 23,000 \text{ ft/s} & : C_D \leq 0.5 \end{cases} \tag{4}$$

$$t_{delay} = \begin{cases} 5 \text{ s} & : L/D < 1.05 \\ 250\,(L/D - 1.05) + 5 \text{ s} & : L/D \geq 1.05 \end{cases} \tag{5}$$

3. Downrange Targeting Phase

After the energy depletion phase, the remaining control authority is used to steer the vehicle to the target location. During this phase, targeting is performed using the NPC. The peak heat rate and g-loading values are computed for each trajectory solution. If the peak values violate their corresponding constraints, then the bank angle is limited to satisfy the active constraint. This is accomplished by identifying a constant bank angle that enables the vehicle to fly along the constraint in the same manner as performed in the energy depletion phase. The vehicle is commanded to fly along this constraint until the bank angle required for range targeting results in a departure from the active constraint.

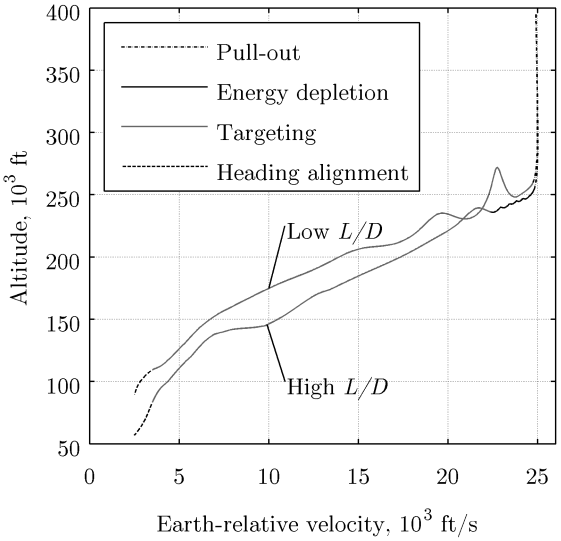

Figure 4. Comparison of guidance phases for low- and high-L/D trajectories.

For low-L/D trajectories, the downrange targeting phase is executed after a small delay that follows the pull-out phase as shown in Fig. 4. In these cases, the low-L/D is a consequence of higher trim-α profiles that increase the drag of the vehicle. As a result, lofted trajectories are required to extend the flight range to ensure delivery to the target. For these trajectories, the downrange targeting phase is initiated at a high velocity. To prevent large changes in bank angle during the initial loft when the dynamic pressure is low, the bank angle is limited to 30 deg $\leq \phi \leq$ 150 deg. Alternatively, high-L/D trajectories require substantial energy depletion and perform no lofting as the NPC guides the vehicle to low altitudes to achieve sufficient deceleration and prevent overshoot of the target. The algorithm transitions from the downrange targeting phase to the heading alignment phase when the vehicle has decelerated to an Earth-relative velocity of 3500 ft/s.

4. Heading Alignment Phase

The heading alignment phase is used to maintain altitude and provide a more shallow flight-path angle to ensure a smooth transition to TAEM. This is accomplished by limiting the magnitude of the bank angle

command to less than 45 deg while continuing to execute the downrange targeting logic. This ensures that the majority of the lift is in the vertical direction, while reserving enough lateral control authority to enable the vehicle to point its velocity vector towards the target. Due to the short amount of remaining time before TAEM initiation, the vehicle does not have the capability to substantially influence the downrange flown during this phase. The guidance algorithm terminates at the end of heading alignment at 2,500 ft/s Earth-relative velocity, and control is notionally handed off to a TAEM algorithm.

C. Lateral Guidance

Since the vehicle is flying at undeflected trim α and the vertical lift magnitude is controlled by the longitudinal channel, the only control parameter available for lateral (crossrange) control is the sign of the out-of-plane component of the lift. This is controlled through bank reversals. Crossrange is managed by limiting the azimuth error. The maximum allowable azimuth error defines a corridor that decreases with velocity; this ensures that the crossrange error decreases as vehicle range control authority decreases during entry. A bank reversal is triggered when the azimuth error exceeds the corridor boundary. The initial azimuth error corridor width is decreased to force an early bank reversal for high-L/D cases. Bank reversals are performed in a shortest-time manner. The lateral corridor and a sample entry trajectory are shown in Fig. 5. In this example, four bank reversals are performed.

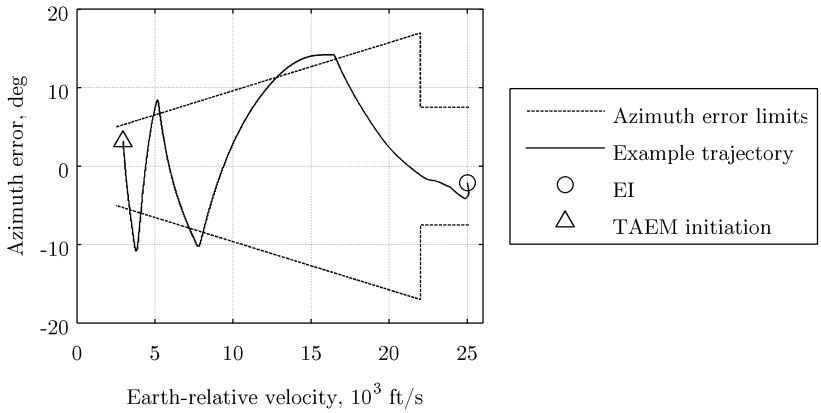

Figure 5. Example entry guidance lateral corridor with entry trajectory.

D. Parameter Estimation

The guidance algorithm uses available navigation data to estimate current aerodynamic parameter values at the start of each guidance cycle. These estimates are used to compute correction factors to the onboard vehicle aerodynamics model. The nominal onboard model consists of a table of C_L and C_D at nominal trim α, as well as the ΔC_L and ΔC_D for expected maximum high and low trim α, all as a function of Mach number. The correction factors, in conjunction with the onboard aerodynamics model, are able to capture shape changes in the trim aerodynamic coefficient curves and significantly improve prediction accuracy. This functionality was developed because existing constant-bias parameter estimation methods, such as those used in the PredGuid algorithm,[21] did not provide sufficient accuracy.

First, an estimate of the L/D is determined from the tangent of the angle between the opposite of the wind-relative velocity vector and the aerodynamic acceleration vector, as shown in Fig. 6 and Eq. (6) and (7). The drag acceleration is then estimated from Eq. (8) and used to estimate the current C_D with Eq. (9) using the density from the onboard atmosphere model. The current C_L is then estimated from the L/D and C_D, as shown in Eq. (10). The estimates of the current C_L and C_D are then used to compute correction factors for each coefficient. The correction factor is given by Eq. (11), where positive values indicate a higher-than-nominal value, negative values indicate a lower-than-nominal

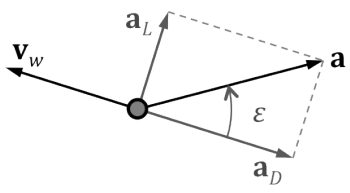

Figure 6. L/D is estimated from navigated velocity and acceleration vectors.

value, and X is a placeholder denoting either lift or drag. The factors are bounded by suitable minimum and maximum values and filtered with previous values using the low-pass filter in Eq. (12) before being stored for use by the predictor. A filter gain, K, of 0.2 has been found to provide an acceptable balance between accuracy and noise. An example of an estimated C_D curve for $F_D = -0.5$ is shown in Fig. 7.

Several assumptions limit the accuracy of this estimation technique. First, in the absence of a flush air data system, the wind-relative velocity is not available from navigation. Instead, the wind-relative velocity is approximated by the Earth-relative velocity. Second, the aerodynamic acceleration is vector is not known precisely; it is approximated with the sensed acceleration vector. This is generally a good assumption, as aerodynamic forces dominate throughout entry and the filter is able to remove most transients caused by the RCS and aerosurfaces. Lastly, this method assumes the onboard atmospheric density model is correct, as density and C_D cannot be separated in the equations of motion when only acceleration and velocity are known.

$$\varepsilon = \operatorname{acos}\left(\frac{-\mathbf{v}_w^T\mathbf{a}}{||\mathbf{v}_w||\ ||\mathbf{a}||}\right) \tag{6}$$

$$L/D_{est} = \tan(\varepsilon) \tag{7}$$

$$a_D = \frac{||\mathbf{a}||}{\sqrt{(L/D_{est})^2 + 1}} \tag{8}$$

$$C_{D,est} = \frac{2ma_D}{v_w^2 S_{ref}\rho_{atm}} \tag{9}$$

$$C_{L,est} = L/D_{est} \cdot C_{D,est} \tag{10}$$

$$F_X = \frac{C_{X,est} - C_{X,nom}(M)}{\Delta C_X(M) - C_{X,nom}(M)} \tag{11}$$

$$F_i = (1-K)\,F_{i-1} + K \cdot F_{est} \tag{12}$$

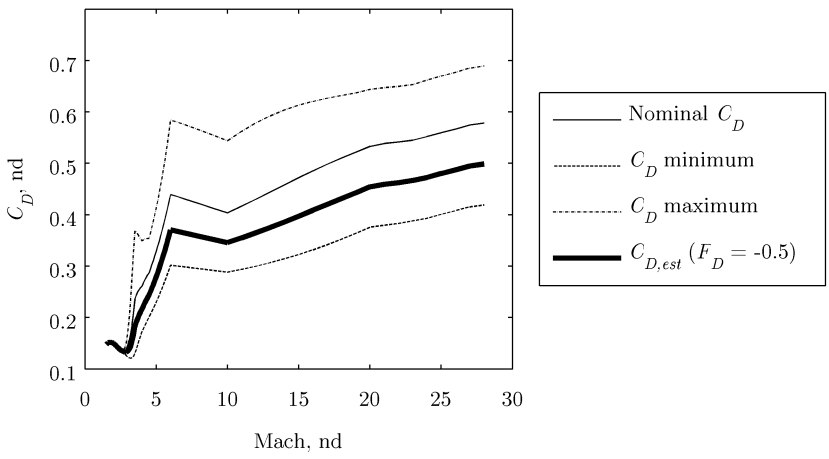

Figure 7. Example of estimated C_D as a function of Mach number.

IV. Results and Discussion

A. Nominal and Stress Case Performance

Nominal entry trajectory performance at undeflected-LBF trim α for ascending and descending approaches to KSC is shown in Fig. 8 and Table 4. Figure 8(b) shows only a small loft is required to limit the peak heat rate and provide the required downrange to reach the target. Figure 8(d) shows small flight-path angles are maintained through the bulk of the hypersonic phase, illustrating the long, low-deceleration equilibrium glide possible with a lifting body. All constraints are satisfied for both approaches. The primary difference between the trajectories is a more flattened g-pulse exhibited by the descending approach, caused by the longer entry range associated with this trajectory.

The bank command and response histories for the ascending and descending approaches are shown in Fig. 9(a) and (b), respectively. The histories are similar: the initial bank command of 0 deg quickly transitions to a near lift-neutral command of approximately 75 deg during the energy depletion phase. The guidance transition to range targeting is easily seen near 24,000 ft/s where the bank command magnitude becomes relatively constant near 50 deg as the guidance algorithm solves the constant bank range problem. The ascending approach performs 6 bank reversals; the descending performs 5. This compares well to STS, which typically performs 4 reversals.[22] Immediately prior to TAEM initiation, the vehicle banks to a near lift-up orientation while maintaining a small amount of heading control. This pull-up maneuver unloads the vehicle (see Fig. 8(c)) and provides a clean transition to the TAEM phase.

The minimum- and maximum-L/D stress cases were analyzed using the ascending approach trajectory. The maximum-L/D stress case uses the maximum expected forward x-c.g. shift (1.5 in) and the minimum expected value of C_M, resulting in lower trim-α values; the minimum-L/D stress case has the opposite properties, resulting in higher trim-α. Trajectory performance results are given in Table 4. Figure 10 shows the resultant trajectories compared to the nominal ascending approach trajectory. All three trajectories are able to reach the target while limiting peak deceleration (Fig. 10(b)) and peak heat rate (Fig. 10(d)) to their constraint values despite radically different trim-α profiles (Fig. 10(a)) and associated L/D profiles (Fig. 10(c)). In particular, the algorithm effectively limits the heat rate for the maximum-L/D case by holding the rate near constant at about 76 BTU/(ft^2·s) until the vehicle has passed though the region of peak heating. In contrast, the guidance algorithm commands a loft for the minimum-L/D case to extend the flight range of this high-drag case.

Table 4. Nominal and Stress Case Trajectory Performance

Parameter	Nominal	Maximum-L/D	Minimum-L/D
L/D at Mach 25	1.05	1.14	0.97
Peak deceleration, g	2.29	2.42	2.20
Peak heat rate, BTU/(ft^2·s)	74.0	76.6	71.0
Integrated heat load, BTU/ft^2	7.18×10^4	8.39×10^4	6.33×10^4
TAEM range error, nmi	2.78	1.38	1.18

B. Dispersed Performance

Monte Carlo simulations were performed to assess the feasibility of the proposed entry strategy by determining vehicle performance in the presence of day-of-flight uncertainties. Summary results are provided in Table 5 for ascending and descending approaches to KSC. Trajectory plots showing the Monte Carlo samples in grey and nominal trajectory in black are shown for the ascending approach in Fig. 11 and Fig. 12.

The spread in L/D profiles created by the variation in trim α due to uncertainties creates a significant challenge for the onboard guidance algorithm. Figure 11(a) shows the range of trajectories commanded by the guidance algorithm to reach the landing site for the ascending approach. Small lofts are required for low-L/D samples, while the high-L/D samples dive deeper into the atmosphere. The bank command histories in Fig. 11(b) show the range of commands necessary to execute the trajectories. While some general trends in the command histories are apparent, some samples require lift-down segments early in the trajectory to reach the desired heat rate while other trajectories, typically those with low C_D, tend fly more

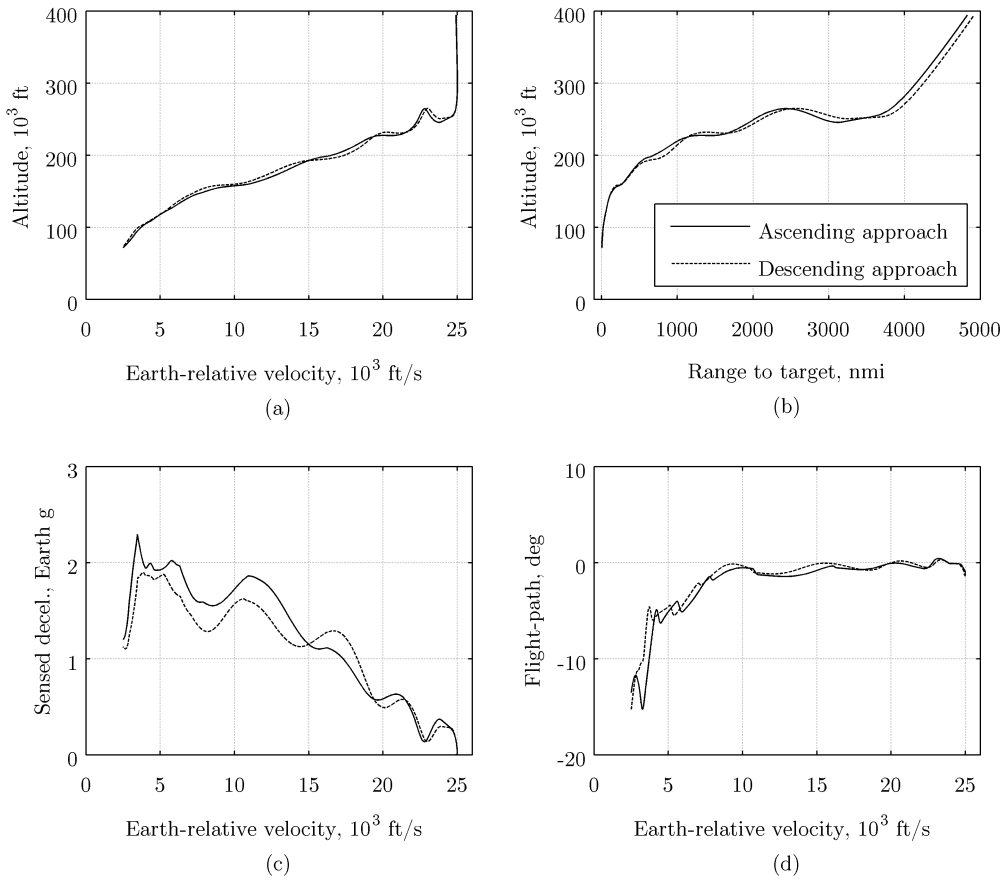

Figure 8. Nominal entry trajectory performance for ascending and descending approaches to KSC: (a) altitude, (c) deceleration, (d) flight-path angle versus velocity; (b) altitude versus range to target.

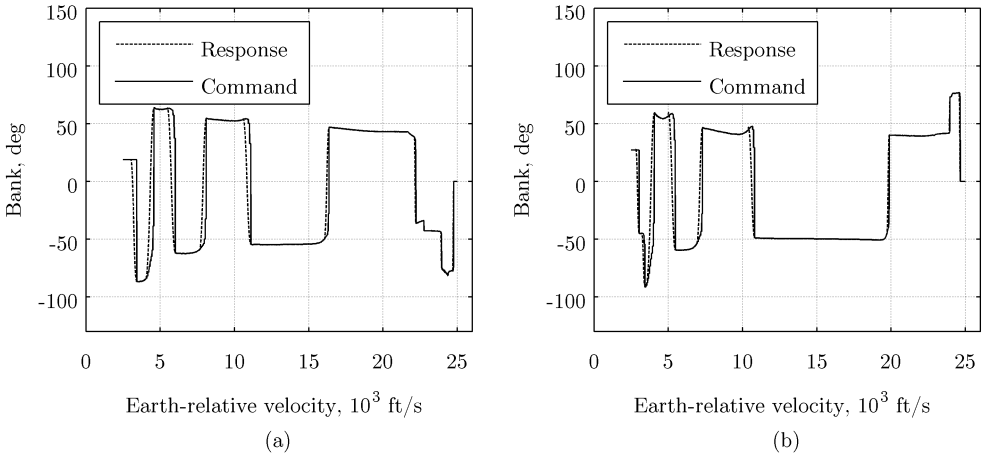

Figure 9. Nominal bank command and response for (a) ascending and (b) descending approaches to KSC.

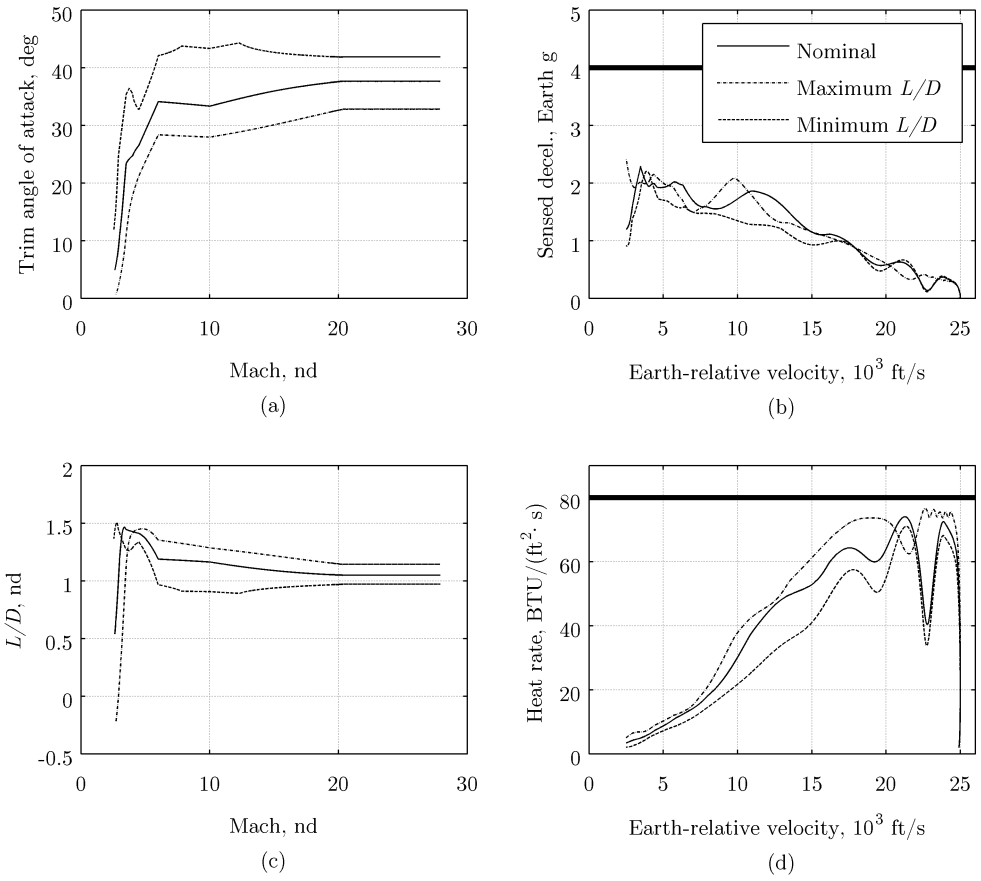

Figure 10. Nominal and stress case entry trajectory performance: (a) α and (c) L/D versus Mach number; (b) deceleration and (d) heat rate versus velocity.

lift down orientations late in the trajectory to avoid overshooting the target. However, as seen in the nominal trajectories in Section A, Fig. 12(a) shows that the algorithm effectively limits the deceleration to below 4 g, with most samples below 2.5 g. The algorithm is also able to limit the peak heat rate: only a single sample violates the 80 BTU/(ft^2·s) limit, and only by a small amount (Fig. 12(b)). Integrated heat loads are also well below the required limit (see Table 5).

While the mean plus three-standard-deviation value of 4.92 nmi for the ascending approach is within the accuracy requirement, the mean plus three-standard-deviation value for the descending approach of 5.82 nmi exceeds the requirement. The TAEM range error exceeds 5 nmi for 4 and 17 samples for the ascending and descending approaches, respectively. However, these misses are small, with maximum values of 5.63 and 6.75 nmi for the ascending and descending approaches, respectively. These misses are not caused by control saturation, but are artifacts of the guidance scheme. First, the guidance algorithm does not attempt to null crossrange error. This strategy greatly simplifies the algorithm by allowing the lateral guidance to be fully decoupled from the longitudinal guidance, but it forces the guidance and mission designers to choose between terminal accuracy and excessive bank reversals near the end of the trajectory. However, even this choice is limited: additional bank reversals introduce additional excursions from the longitudinal bank command, further degrading accuracy. Second, the algorithm's numeric predictor uses simplified two-dimensional equations of motion over a spherical Earth. While geodetic target coordinates have been converted to their geocentric equivalent for the algorithm, the assumptions inherent in using the reduced-order equations of motion over a spherical Earth introduce error into the guidance algorithm's knowledge of the target location, even when perfect navigation knowledge is assumed. Lastly, irrespective of the accuracy requirement, appropriately designed TAEM and approach and landing algorithms can steer out the errors present at TAEM initiation.

Overall, the developed guidance algorithm shows good performance, indicating that it is feasible to fly a lifting body without steady-state LBF deflections. However, even small steady-state deflections of 5 deg may significantly reduce the range of trim-α profiles the guidance algorithm must accommodate, potentially improving performance and increasing system margin.

Table 5. Monte Carlo Results

Parameter	Ascending approach				Descending approach			
	Mean	Std. dev.	Min.	Max.	Mean	Std. dev.	Min.	Max.
L/D at Mach 25	1.05	0.0382	0.956	1.17	1.05	0.0382	0.956	1.17
Peak deceleration, g	2.33	0.177	1.94	3.62	2.11	0.193	1.60	3.92
Peak heat rate, BTU/(ft^2·s)	74.3	1.78	69.7	80.5	73.1	2.74	65.7	80.3
Heat load, 10^4 BTU/ft^2	7.21	0.417	6.24	8.48	7.28	0.417	6.29	8.63
TAEM range error, nmi	2.25	0.889	0.0838	5.63	2.46	1.12	0.155	6.75
TAEM altitude, 10^3 ft	71.2	0.791	50.9	90.8	72.6	8.08	53.8	92.6

C. Mission Design Flexibility

In addition to uncertainty analysis, the robustness of undeflected-LBF flight performance was evaluated through parametric scans related to mission design quantities of interest. First, the target latitude and longitude coordinates were varied to evaluate nominal guided range capability. Second, the EI Earth-relative velocity and flight-path angle were varied about the nominal ascending approach EI point to determine the size of the entry corridor.

The range capability with undeflected LBFs is shown in Fig. 13. The guided range capability is defined to be the locus of target locations for which the vehicle meets all constraints. In this case, only the accuracy and deceleration constraints are active; the peak heat rate and heat load constraints do not limit the range capability. From the nominal ascending EI point, the downrange capability covers approximately 1900 nmi, with shorter and longer downranges possible for landing sites off the centerline of the range capability. The maximum crossrange is approximately ±660 nmi. While this crossrange capability is less than STS requirement of ±750 nmi,[23] it still provides operational flexibility for crew return from LEO and offers significant performance benefits over capsule-type entry vehicles, which typically have a maximum crossrange

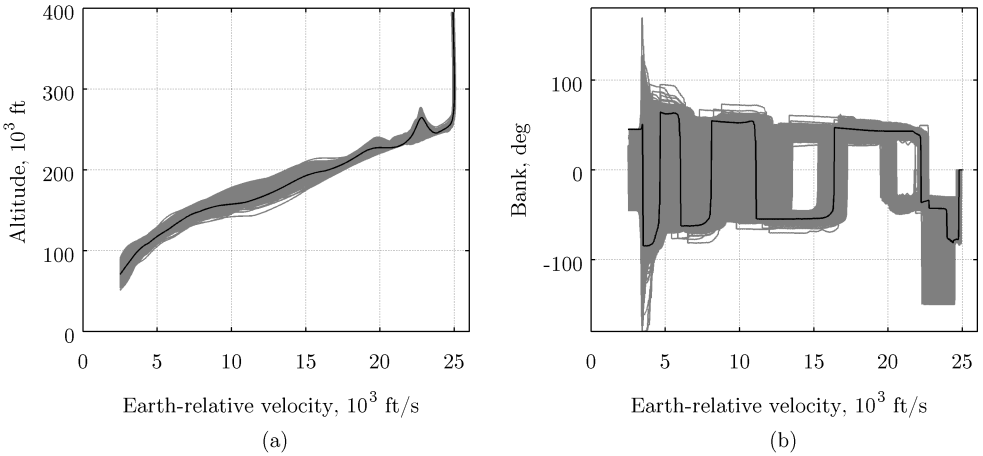

Figure 11. Dispersed (grey) and nominal (black) trajectories: (a) altitude and (b) bank angle command versus Earth-relative velocity.

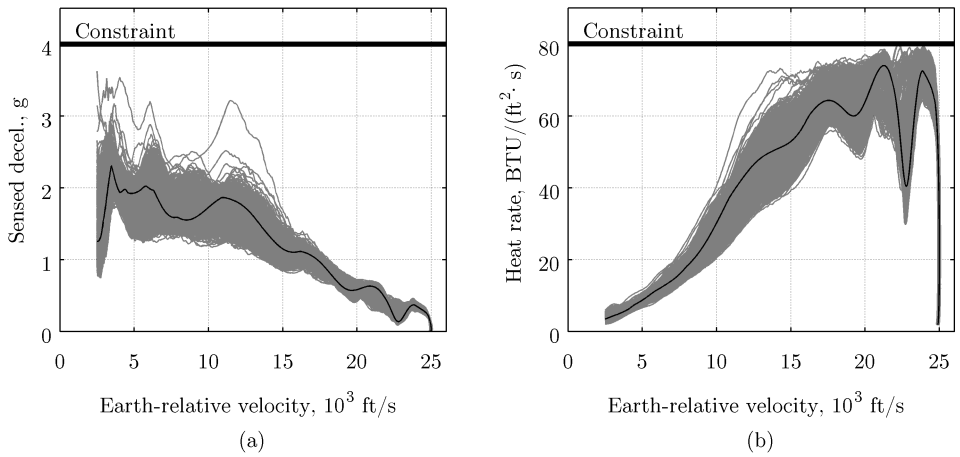

Figure 12. Dispersed (grey) and nominal (black) trajectories with constraints: (a) deceleration and (b) heat rate versus Earth-relative velocity.

below ±100 nmi.[24] If necessary, crossrange can be improved by increasing vehicle L/D, relaxing trajectory constraints, imposing EI state constraints, or providing α control. The range capability is offset in crossrange in Fig. 13 due to an initial offset in crossrange at the ascending approach EI point. The results shown are for nominal conditions only; operational range capability will be reduced from that shown in Fig. 13.

Figure 14 shows the nominal corridor available for deorbit targeting about the nominal ascending approach EI point, i.e. the set of acceptable EI Earth-relative velocity and flight-path angle states for which the vehicle can reach the nominal target while satisfying all trajectory constraints. The figure shows that the feasible space is bounded by the heat rate constraint on the undershoot side and the nearly coincident accuracy and deceleration constraints on the overshoot side. As seen in previous sections, the heat load constraint is not limiting and the deceleration constraint has only a small effect on the size of the feasible region. Additionally, the nominal ascending approach EI state is roughly centered in the feasible region, indicating that it was appropriately selected. Independent of other constraints, the accuracy performance was evaluated over the same set of EI Earth-relative velocities and flight-path angles for three different target ranges. The results are shown in Fig. 15. The plot shows several trends. First, the corridor size expands for shorter target ranges, as well as for steeper entry flight-path angles. The plot also shows a general deterioration of accuracy performance for shorter target ranges with higher energies and steeper flight-path angles. This is expected, as the vehicle has only a short period of time to effectively manage its energy to reach the target. Lastly, Fig. 15 shows results independent of other constraints: the consideration of peak heat rate and peak deceleration constraints will significantly shrink the size of the corridor, as shown in Fig. 14.

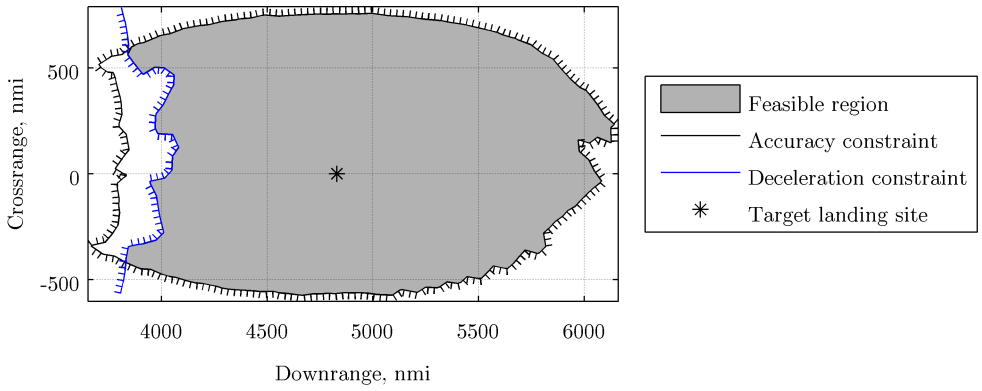

Figure 13. Range capability from ascending approach.

V. Conclusion

The results presented show that entry with undeflected LBFs is feasible for a reasonable set of trajectory constraints. This validates the entry strategy as well as the capabilities of the developed guidance algorithm, especially its ability to estimate vehicle aerodynamic properties and then select commands to satisfy all constraints. The results confirm that lifting bodies possess a high level of robustness to day-of-flight uncertainties and a degree of flexibility in mission design that blunt body capsule vehicles do not possess. Entry trajectory performance improvements may be possible with additional algorithm development. First, moving to a full three-degree-of-freedom predictor will improve prediction accuracy and eliminate the need for a Coriolis correction, but at additional computational cost. Second, many guidance parameters were set to reduce the impact of the development status of the algorithm on entry performance, including iteration limits, heat rate control parameters, and crossrange error bounds. Optimizing these parameters with respect to performance metrics of interest, such as the total number of bank reversals, will also improve performance.

Zeroing or minimizing steady-state LBF deflections provides several benefits to a lifting body entry vehicle. Most importantly, minimizing LBF deflections reduces the severity of the aerothermal environment on the LBFs, the primary goal of this feasibility study. Second, the absence of steady-state deflections frees

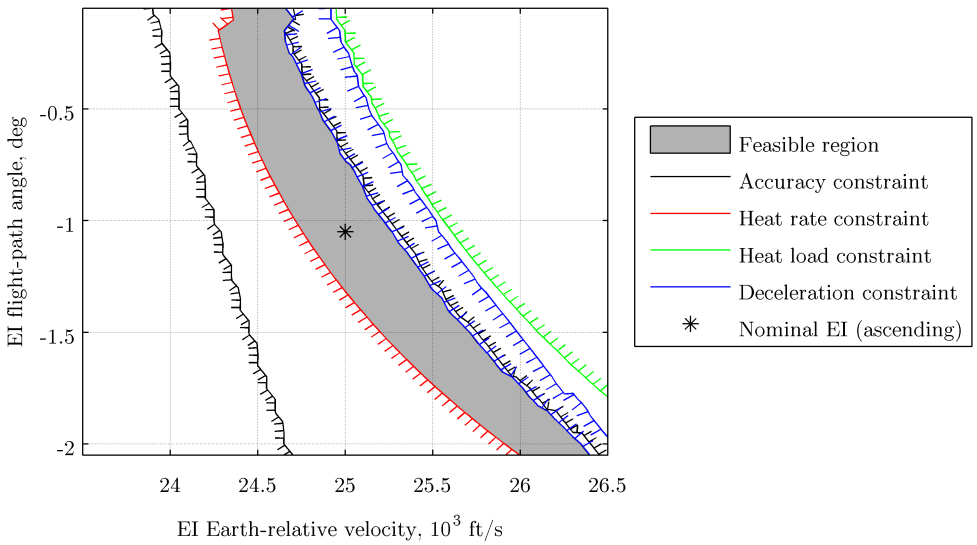

Figure 14. Velocity-flight-path angle entry corridor for ascending approach.

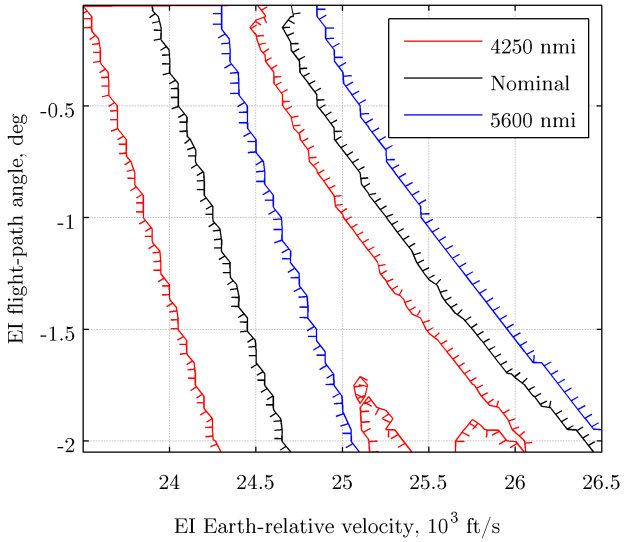

Figure 15. Velocity-flight-path angle entry corridor for ascending approach for three flight ranges.

the full control power of the aerosurfaces for use in transient maneuvers, improving control power margin. This is significant, as even when α control is used, bank control is the primary means of steering for most entry vehicles. This improvement in control power margin may be used to either improve transient maneuver response times or to reduce the mass of the aerosurfaces by imposing more strict deflection limits, allowing use of a less massive TPS, or by reducing the size of the aerosurfaces.

While lifting body entry without steady-state LBF deflections has been shown to be feasible, small steady-state deflections may be used judiciously to reduce the range of α profiles that must be accommodated by the guidance algorithm and mission designers. Small LBF deflections will likely avoid severe aerothermal conditions on the flaps and may be used to improve entry performance or overall entry system margins. Steady-state LBF deflections may also be used after the heat pulse in the low hypersonic and supersonic regimes when aerosurface heating is no longer a concern. This strategy may provide notable performance improvements.

Acknowledgement

This work was performed under contract from the Sierra Nevada Corporation.

References

[1]Stone, H. W. and Piland, W. M., "21st century space transportation system design approach - HL-20 personnel launch system," *Journal of Spacecraft and Rockets*, Vol. 30, No. 5, Sept. 1993, pp. 521–528.

[2]Harpold, J. C. and Graves, C. A., "Shuttle Entry Guidance," Tech. Rep. NASA-TM-79949, NASA, Houston, Texas, Feb. 1979.

[3]Gamble, J. D., Cerimele, C. J., Moore, T. E., and Higgins, J., "Atmospheric Guidance Concepts for an Aeroassist Flight Experiment," *Journal of the Astronautical Sciences*, Vol. 36, No. 1/2, Jan. 1988, pp. 45–71.

[4]Rea, J. R. and Putnam, Z. R., "A Comparison of Two Orion Skip Entry Guidance Algorithms," *AIAA Guidance, Navigation, and Control Conference*, Hilton Head, SC, Aug. 2007.

[5]McNamara, L. W., "Entry Atmospheric Flight Control Authority Impacts on GN&C and Trajectory Performance for Orion Exploration Flight Test 1," *AIAA Guidance, Navigation, and Control Conference*, Minneapolis, Minnesota, Aug. 2012.

[6]Vincenty, T., "Direct and Inverse Solutions of Geodesics on the Ellipsoid with Application of Nested Equations," *Survey Review*, Vol. XXII, No. 176, April 1975, pp. 88–93.

[7]Justus, C. G. and Leslie, F. W., "The NASA MSFC Earth Global Reference Atmospheric Model—2007 Version," Tech. Rep. NASA-TM-2008-215581, NASA, Nov. 2008.

[8]Chapman, D. R., "An Approximate Analytical Method for Studying Entry Into Planetary Atmospheres," Tech. Rep. R-11, Ames Research Center, 1959.

[9]Tauber, M. E. and Sutton, K., "Stagnation-point Radiative Heating Relations for Earth and Mars Entries," *Journal of Spacecraft and Rockets*, Vol. 28, No. 1, June 2003, pp. 40–42.

[10]Ware, G. M. and Cruz, C. I., "Aerodynamic Characteristics of the HL-20," *Journal of Spacecraft and Rockets*, Vol. 30, No. 5, Sept. 1993, pp. 529–536.

[11]Powell, R. W., "Six-Degree-of-Freedom Guidance and Control-Entry Analysis of the HL-20," *Journal of Spacecraft and Rockets*, Vol. 30, No. 5, Sept. 1993, pp. 537–542.

[12]Howard, R. D., Krevor, Z. C., Mosher, T., Scott, K. P., Voss, J. S., Sanchez, M. J., and Curry, J. M., "Dream Chaser Commercial Crewed Spacecraft Overview," *17th AIAA International Space Planes and Hypersonic Systems and Technologies Conference*, April 2011.

[13]Ehrlich, K. F., "HL-20 Concept: Design Rationale and Approach," *Journal of Spacecraft and Rockets*, Vol. 30, No. 5, Sept. 1993, pp. 573–581.

[14]Wurster, K. E. and Stone, H. W., "Aerodynamic Heating Environment Definition/Thermal Protection System Selection for the HL-20," *Journal of Spacecraft and Rockets*, Vol. 30, No. 5, Sept. 1993, pp. 549–557.

[15]Lee, D. L., "Constellation Program Human-Systems Integration Requirements," Tech. Rep. CxP 70024, Nov. 2010.

[16]D'Souza, C. D., Crain, T., Clark, F. D., and Getchius, J., "Orion Cislunar Guidance and Navigation," *AIAA Guidance, Navigation and Control Conference adn Exhibit*, Hilton Head, SC, Aug. 2007, pp. 1–21.

[17]Gamble, J. D. and Young, J. C., "The Development and Application of Aerodynamic Uncertianties in the Design of the Entry Trajectory and Flight Control System of the Space Shuttle Orbiter," *9th AIAA Atmospheric Flight Mechanics Conference*, NASA Johnson Space Center, San Diego, CA, June 2003, pp. 1–14.

[18]Vanderplaats, G. N., *Numerical Optimization Techniques for Engineering Design*, Vanderplaats Research and Development, Inc., 2005.

[19]Brent, R. P., *Algorithms for Minimization without Derivatives*, Prentice-Hall, 1972.

[20]Powell, R. W. and Cruz, C. I., "Guidance and Control Analysis of the Entry of a Lifting Body Personnel Launch Vehicle," *29th AIAA Aerospace Sciences Meeting*, Reno, NV, Jan. 1991.

[21]Bairstow, S. H. and Barton, G. H., "Orion Reentry Guidance with Extended Range Capability Using PredGuid," *AIAA Guidance, Navigation, and Control Conference*, Hilton Head, South Carolina, Aug. 2007, pp. 1–17.

[22]Harpold, J. C. and Gavert, D. E., "Space Shuttle Entry Guidance Performance Results," *Journal of Guidance*, Vol. 6, No. 6, Nov. 1983, pp. 442–447.

[23]Joosten, B. K., "Descent Guidane and Mission Planning for Space Shuttle," *Space Shuttle Technical Conference*, NASA Johnson Space Center, Jan. 1985, pp. 113–124.

[24]Reding, J. P. and Svendsen, H. O., "Lifting Entry Rescue Vehicle Configuration," *Journal of Spacecraft*, Vol. 27, No. 6, Nov. 1990, pp. 606–612.